Investigations of structure-improper ferroelectricity relationships to enhance the multifunctional applications of the β′-Y$_2$(MoO$_4$)$_3$ phase

G. Gil-de-Cos [a,*], M.E. Torres [a,b], C. González-Silgo [a,b]

[a] *Departamento de Física, Universidad de La Laguna, Apdo 456, E-38200, San Cristóbal de La Laguna, Santa Cruz de Tenerife, Spain*
[b] *Instituto Universitario de Materiales y Nanotecnología IMN, Universidad de La Laguna, La Laguna, Tenerife, 38200, Spain*

ARTICLE INFO

ABSTRACT

Polycrystalline samples of the compound Y$_2$(MoO$_4$)$_3$ have been synthesized by solid-state reaction starting from the corresponding yttrium and molybdenum oxides, and the pure ferroelectric phase has been successfully isolated. Both β' (ferroelectric) and β (paraelectric) phases were studied by conventional X-ray diffraction at different temperatures, performing the corresponding Rietveld refinements before and after the phase transition. An analysis of the displacive symmetry modes involved was carry out. The thermal dependence of the crystal structure was also studied, confirming that it is an improper ferroelectric with a primary order parameter that does not correspond to the spontaneous polarization. To corroborate the purity of the β′-phase, TG and SEM-EDX analyses were performed, demonstrating the absence of the γ-phase. Moreover, DSC analysis and impedance spectroscopy confirmed the Curie temperature of the β′-β phase transition (T$_c$ around 378 K). Ferroelectric hysteresis cycles were recorded as a function of temperature and at different maximum applied electric fields. The values of the maximal and remanent polarization were correlated with the structural study. Finally, anomalies in the electrical permittivity and conductivity were observed between 600 and 877 K, which may be associated with the evolution of the lattice parameter *c* at high temperatures. With this ferroelectric characterization we want to highlight this still unexploited crystal matrix in comparison to other rare earth molybdates with the β′-phase and other yttrium molybdate compounds.

1. Introduction

Compared to borates, silicates, sulfates, phosphates or vanadates; rare earth doped oxomolybdates (VI) and tungstates have attracted more attention in the last two decades for luminescence applications (emissive screens, fluorescent lamps and LEDs, and systems to detect X-rays or γ-rays, etc.) due to their lower lattice vibration energy, high thermal and electrical stability, and high UV absorption of MO$_4^{2-}$ oxoanion (M = W, Mo) [1,2]. These compounds, with optically inactive cations (Y^{3+}, La^{3+}, Gd^{3+} and Lu^{3+}), are suitable host matrices for inserting active rare earth that remain stable and uninfluenced by environmental conditions [3–6]. In this context, several yttrium molybdate phosphors have been prepared and studied during the last decade. For example, the high efficiency of Eu^{3+} doped matrices: Y$_2$Mo$_4$O$_{15}$ and Y$_2$Mo$_3$O$_{12}$ has been demonstrated [7–9]. Moreover, tunable luminescence by doping with other lanthanides (Sm, Dy) in Y$_2$(MoO$_4$)$_3$, Y$_2$MoO$_6$ matrices [10–13], and up-conversion properties in co-doped phosphors (Er^{3+}/Yb^{3+} and Ho^{3+}/Yb^{3+}) [14–16] increase its interest.

Also, molybdenum (Mo)-based materials are promising as high-performance materials for electrochemical energy storage devices (fuel cells, batteries and supercapacitors), which are increasingly in demand. For example, among the materials used as solid electrolytes, the family of fast ionic conductors, La$_{2-x}$RE$_x$Mo$_{2-y}$W$_y$O$_9$ (RE ≡ Ln and Y), is among the most studied [17]. In addition, rare earth tungstates and molybdates with the general formula RE$_2$Mo$_3$O$_{12}$ (RE ≡ Ho–Lu and also Y, Sc, Al) exhibit unusually high trivalent ion conduction [18]. More recently, nanostructures of Y$_2$(MoO$_4$)$_3$ nanowires and nanosheets, have been investigated as candidates for anode fabrication [19,20]. Furthermore, the ionic conductivity in new triple molybdates is being investigated [21,22].

The new and improved functionalities targeted by research in both fields (related to those mentioned above optical and electrical properties) can only be fulfilled with a thorough understanding of the relationship between the structure and properties of these crystalline materials. In the case of yttrium oxomolybdates, there are several compounds belonging to four chemical formulas whose crystal structures have been investigated. The correlations of structure and optical properties of Y$_2$MoO$_6$

(with space group *C2/c* and Z = 4) have been studied [13,23]. More recently, Guzik et al. [24] have presented and discussed the structural and spectroscopic properties of the new transparent ceramic $Y_2Mo_2O_9$, which crystallizes in the cubic system (space group *P2₁3*, Z = 2). Molybdates with the formula $RE_2Mo_4O_{15}$ adopt four different structures; when RE ≡ Tb–Lu and Y, they are monoclinic (with space group *P2₁/c*, Z = 2) and exhibit negative thermal expansion in the temperature range of 298–443 K [25]. The most investigated group of molybdates with rare earth and trivalent metals has the formula $RE_2(MoO_4)_3$ (RE ≡ La–Lu), which crystallizes in various polymorphs depending on ionic radii and synthesis conditions. This rich polymorphism becomes evident under changes in pressure and temperature [26,27].

In particular, for $Y_2(MoO_4)_3$, two polymorphs coexist at room temperature, which are not symmetrically equivalent [28]. The γ-phase with space group *Pbcn* and Z = 4 (γ-$Sc_2(WO_4)_3$ type structure) is hydrated at ambient conditions, complicating low-temperature studies. The main property of this phase is its negative thermal expansion with large negative values of the coefficient of linear expansion after the complete removal of the water molecules [29–31]. The second polymorph grows with the β'-$Gd_2(MoO_4)_3$-type structure (space group *Pba2* and Z = 4), which belongs to a well-known family of improper ferroelectrics and ferroelastics [26,32]. In this group of rare-earth molybdates (RE ≡ Pr–Ho, Y), the spontaneous polarization and deformation disappear after the β'-β phase transition. The paraelectric and paraelastic phase (β-phase) crystallizes in the *P-42₁m* space group with Z = 2. Its most exploited properties are probably related to the lack of the center of symmetry, with potential applications in nonlinear devices: piezoelectrics and electro-optical devices [33,34], laser frequency doublers, and filters [35]. More recently, the multiferroic properties have been exploited in β'-$Gd_2(MoO_4)_3$ thin films [36,37]. Moreover, the spontaneous polarization of improper ferroelectrics (secondary order parameter) is subject to the same electrostatics as in their "proper" counterparts but complemented by additional functionalities derived from the primary order parameter that can give rise to new functionalities specific to these materials [38,39]. Of course, these matrices have been widely used as phosphors, which are good hosts for rare-earth ions, as it has mentioned above.

In the case of the yttrium oxomolybdate, as for the holmium molybdate [40], the γ-phase has kinetic preference over the formation of the β' phase, thermodynamically stable below 823 K [28]. Therefore, above this temperature, the γ-$Y_2(MoO_4)_3$ isomorph is more stable. This indicates that the preparation by solid-state, sol-gel, hydrothermal, etc., synthesis of the pure β'-$Y_2(MoO_4)_3$ isomorph is complex. It should be recalled that for the other $RE_2(MoO_4)_3$ ferroelectrics (RE ≡ Pr, Nd, Sm, Eu, Gd, Tb, and Dy), the β-phase is more stable at high temperatures, with the α-phase being the most stable at low temperature [26]. This phase adopts the space group *C2/c* with Z = 4, corresponding to the α-$Eu_2(WO_4)_3$ structure type, which belongs to the modulated scheelite family [41]. In addition, the α-γ phase transition has also been described for rare-earth tungstates [including $Y_2(WO_4)_3$] [42]. Tungstates with this stoichiometry have not been found with the β'-phase which is unique to molybdates.

In this work, we are interested in the synthesis conditions, thermal stability, structural, dielectric and ferroelectric characterization of the pure β'-$Y_2(MoO_4)_3$ phase. Its properties are expected to be similar to those of other isostructural ferroelectrics, in addition to its the interest as a rare earth free compound. The combination of its nonlinear properties, polymorphism and usefulness as a host matrix, make it a fascinating and promising multifunctional material, which has not been fully exploited compared to its isomorph (the γ-phase) and other improper ferroelectrics, with the β'-$Gd_2(MoO_4)_3$ phase.

2. Experimental

2.1. Synthesis

The β' phase of $Y_2(MoO_4)_3$ was prepared via solid-state reaction from precalcined molybdenum oxide (MoO_3) and yttrium oxide (Y_2O_3)

(Aldrich, 99.99%) for 10 h at 923 and 1173 K, respectively and a heating/cooling rate of 393 K/min. Next, they were weighed in stoichiometric quantities, mixed, and grounded in an agate mortar for at least one and a half hours. Then, the powder resulting from this grinding was compacted in a uniaxial hydraulic press at a pressure of 380 MPa. The resulting pellets were stored in an oven at 423 K for 72 h, then heated at 806 K for 96 h at a heating rate of 513 K/min and cooled to 473 K by quenching (with the furnace at an estimated cooling rate of ~1273 K/min). Then, as mentioned above, the pellets were reground for 1 h and a half, compacted at a pressure of 227 MPa, and subjected to a second heat treatment at 928 K for 48 h at a heating rate of 513 K/min with the following quenching at 393 K (with the furnace at an estimated cooling rate of ~1273 K/min). The total synthesis was carried out in an air atmosphere. Finally, the samples were stored in a desiccator until the subsequent characterization of their physical properties.

2.2. Structural and microstructural characterization

X-ray powder diffraction (XRD) was used to monitor the phase purity and its structural characterization. Diffractograms were collected using a Panalytical Empyrean diffractometer with Cu-Kα radiation [wavelength: λ(Cu-Kα₁) = 1.54056 Å and λ(Cu-Kα₂) = 1.54443 Å] passing through a Ni filter, a fixed slit and a divergence of 1/2° and 1/8°, respectively. Routine and high-temperature measurements were collected at an angular interval of 5°<2θ < 80° with a step of 0.02° and 57 s step time. For the ferroelectric characterization, a graphite monochromator was used, and the angular range was increased to 2θ = 120°, but the time at each step was maintained. Measurements at different temperatures were performed using an Anton Paar TTK-450 chamber in an air atmosphere from 248 to 573 K, leaving the sample for 5 min at the selected temperature before proceeding to the data collection. Data were also collected at higher temperatures, with the first setting from 298 to 773 K [43].

Microstructure and compositional analysis of the obtained pellets were carried out using a ZEISS EVO 15 scanning electron microscope (SEM) with 2 nm resolution, which was coupled to a 50 mm2 Oxford X-MAX energy dispersive X-ray microanalyzer (EDS) [44].

2.3. Thermal stability. Dielectric and ferroelectric characterization

An SDT650 Simultaneous Thermal Analyzer (TA Instruments) was used to study the thermal stability and detect the paraelectric-ferroelectric phase transition temperatures. Simultaneous thermogravimetric analysis (TG/DTG) and differential scanning calorimetry (DSC) was carried out in an inert atmosphere, with continuous nitrogen flow and heating and cooling ramps of 5, and 10 K/min in a temperature range of the cyclic process between 300 and 823 K (TG/DTG) and between 223 and 773 K (DSC) [45].

The dielectric permittivity and conductivity study was carried out in a frequency range from 5 Hz to 13 MHz applying an alternating voltage with a peak value of 0.7 V and in a temperature range from 313 to 600 K, with the aid of an HP 4192A LF Impedance Analyzer. This characterization was performed on 13 mm diameter pellets with thicknesses of 0.6 mm and whose surfaces were coated with platinum dye (6082-Platinum paste-Metalor).

The Polarization-Electric Field ferroelectric hysteresis loop (P-E curve) was recorded by applying a triangular signal with a maximum amplitude of 1600 V and with a period of 500 ms, at different temperatures, using the Precision LC Main Unit with a High Voltage Precision of 10 kV HVI-SC interface and a Teflon cell (HVTF) that allows heating up to 503 K, from Radiant Technologies, Inc [46]. These cycles were recorded on the same pellets used in the dielectric measures.

2.4. Data analysis

2.4.1. Crystal data refinement

Rietveld refinement of the crystal structure was performed with the

Fullprof software [47] from the diffractograms collected at 248, 273, 298, 323, 348 and 373 K. All diffractograms were identified and refined with the ferroelectric β′-Y$_2$(MoO$_4$)$_3$ phase [7,28]. The Thompson-Cox-Hasting pseudo-Voigt profile shape function modeled the experimental profiles and the background was fitted with a Chebyshev polynomial. A correction due to micro absorption was performed since the sample did not have a completely flat surface. In all cases, very small impurities of Y$_2$O$_3$ [48] were observed, and this phase was added to the refinement.

Regarding the crystal structure, the displacements from the paraelectric phase "the ferroelectric distortion" were refined instead of the atomic coordinates. The ferroelectric structures were obtained, analyzing the distortion from the paraelectric phase. The AMPLIMODES software, from the Bilbao Crystallographic Server, relates the two structures based on symmetry-adapted modes and calculates the amplitudes and the polarization vectors of the distortion modes of different symmetry frozen in the less symmetrical structure [49]. The spontaneous polarization can be closely related to the amplitude of some symmetry mode [50]. First, the paraelectric structure was modeled from the known β-Y$_2$(MoO$_4$)$_3$ structure [7] and the same atomic coordinates were refined for two diffractograms collected at 373 K using the "multipattern" mode available in FullProf. Taking this structure as a prototype, the amplitudes of the symmetry modes given by the irreducible representation Γ$_1$, which maintains the symmetry of the prototype phase, were refined for data collected at higher temperatures (423, 473, 523 and 573 K), i.e., with the paraelectric β-phase. In this case, the distortions remain in the same space group. Anisotropic thermal parameters were refined for Y and Mo atoms and isotropic ones for the oxygen atoms.

Next, we refined the ferroelectric phase from diffractograms collected at lower temperatures (248, 273, 298, 323, 348 and 373 K) starting from the previous prototype phase. The "ferroelectric distortion" was decomposed into three symmetry modes [51]: 1) a primary mode corresponds to the irreducible representation M$_2$+M$_4$ associated with the point M (1/2, 1/2, 0) on the boundary of the Brillouin zone. 2) A secondary polar mode in the center of the Brillouin zone with the symmetry given by the irreducible representation Γ$_3$. 3) Finally, another secondary mode given by the irreducible representation Γ$_1$. Some of the amplitudes of these symmetry modes were canceled, which would help to reduce the number of the refinement parameters. This refinement has many advantages, especially in the present case, where the oxygen atoms (with minimal X-ray scattering amplitude) cause the distortions by displacements from the more symmetric phase. Moreover, in this case, the thermal evolution of the total amplitude of the symmetry modes can be correlated with the dielectric and the ferroelectric behavior. Isotropic thermal parameters were refined for all atoms, which were restricted in the case of the oxygen atoms.

As we have commented, the diffractograms collected at higher temperatures, from 298 to 773 K, were measured with lower resolution (non-monochromatic radiation and shorter angular interval). In this case, no structural parameters were refined except for the unit cell. For this, a Le Bail refinement [52] was performed, using the same profile model as in the previous case, and the background was modeled by interpolating several selected points.

2.4.2. Obtaining ε′(ω, T) and σ′(ω, T) curves and adjustments

The dielectric properties, i.e., the real part of the complex permittivity ε′ and conductivity σ′ of yttrium molybdate pellets, were studied by measuring the complex impedance Z*(ω) as a function of frequency for different temperatures. The complex permittivity ε*(ω) was calculated from the obtained value of Z*(ω) according to the following relation:

$$\varepsilon^*(\omega) = \frac{t}{i\omega\varepsilon_0 Z^*(\omega)A_c} \tag{1}$$

where ε$_0$ is the vacuum dielectric constant and A$_c$, the area of the electrode and t is the thickness of the sample. As well, the complex permittivity can be expressed as:

$$\varepsilon^*(\omega) = \varepsilon'(\omega) - i\frac{\sigma'(\omega)}{\omega} \tag{2}$$

where σ′(ω) is the real part of the complex conductivity. The analysis of the conductivity spectra has been performed based on the Universal Dielectric Response (UDR) model, an empirical power law that can describe the frequency and temperature dependence of the dielectric response in a wide range of materials from glasses to ionic glass crystals, non-stoichiometric crystals, polycrystalline and amorphous semiconductors [53–57]. Thus, the real part of the conductivity spectrum σ′(ω) tends towards the direct current conductivity (σ$_{dc}$) as the frequency decreases and shows a dispersive regime in which the conductivity increases strongly with frequency with an exponential dependence at high frequencies [58]. In this work, the following expression is used for this dependence [59]:

$$\sigma'(\omega) = \sigma_{dc}\left[1 + cos\left(\frac{s\pi}{2}\right)\left(\frac{\omega}{\omega_p}\right)^s\right] \tag{3}$$

where, ω$_p$ is the frequency at which a change of slope occurs in the real component of the complex conductivity. The parameter s (Jonscher parameter) ranges from 0 to 1, which depends on many-body interactions between charge carriers. The thermal dependence of the parameters (σ$_{dc}$, ω$_p$, and s) was obtained by fitting the curves of the real part of the conductivity at different temperatures. Together with the permittivity and the electrical conductivity, the transition temperatures and the dynamics followed by the charges and dipoles that contribute to the abnormal behavior around the phase transition were investigates. Following the Arrhenius relationship, a fitted line was also performed to determine the activation energies of the different transition mechanisms and the thermal anomalies.

$$\sigma_{dc} = \sigma_0\, exp\left(-\frac{E_a}{2k_BT}\right) \tag{4}$$

where σ$_0$ is a pre-exponential factor, E$_a$ is the activation energy and k$_B$ is the Boltzmann constant. The thermal dependence of the crystal structure and the dielectric properties were complemented by the thermal analysis
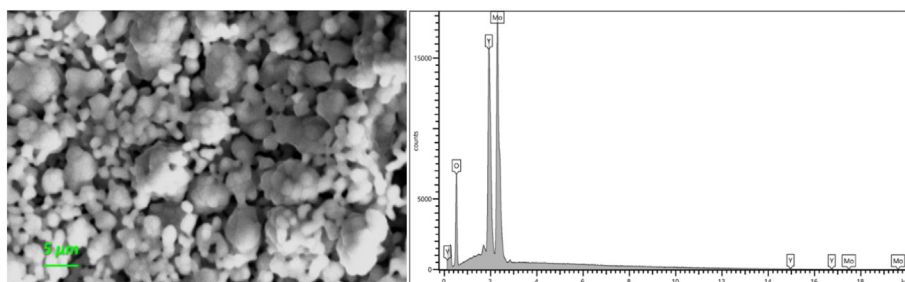

Fig. 1. On the left, SEM image for a Y$_2$(MoO$_4$)$_3$ pellet at a 5 μm scale. On the right is the EDX spectrum of the sintered pellet.

Table 1
Results of compositional analysis by EDX.

Elements	Experimental Values		Theoretical Values	
	Weight (%)	*Atomic (%)*	*Weight (%)*	*Atomic (%)*
O	30.03	71.39	29.189	70.588
Y	27.35	11.71	27.072	11.765
Mo	42.62	16.90	43.772	17.647

and the hysteresis cycles collected at different temperatures.

3. Results and discussion

3.1. Phase identification and SEM-EDX analysis

After several synthesis attempts, the β′ phase, with space group *Pba2* (32) and Z = 4, was identified in the diffraction patterns measured for the sample synthesized under the exposed conditions. All the diffraction peaks matched well with the reported values from the Joint Committee on Powder Diffraction Standards card (JCPDS, 71–0915). Some small Y_2O_3 peaks were also identified (JCPDS, 83–0927) with space group $Ia\bar{3}$ (206) and Z = 16. A purity of 99.7% was calculated after the Rietveld refinement. In previous syntheses, at higher temperatures, the β′-phase appeared mixed with the hydrated γ-phase or with the $Y_2Mo_4O_{15}$ phase when the pellet was subjected to higher pressures and the sintering temperature was lower. Fig. 1, on the left, shows the SEM image of the microstructure of a sintered pellet at a scale of 5 μm and, on the right, the compositional spectrum. This pellet was used in both dielectric and ferroelectric characterization. It can be seen that the approximate grain size is between 1 and 3 μm. In the compositional spectrum, it is observed that the peaks correspond to the elements Y, Mo, and O. From the intensities of these peaks, the relative weight and the atomic fraction percentages were estimated. They are shown in Table 1, together with

the theoretical values. This result indicates the high purity of the synthesized compound.

3.2. Thermal analysis

TG-DTG and DSC curves for $Y_2(MoO_4)_3$ obtained during a heating-cooling cycle are shown in Fig. 2a and Fig. 2b, respectively. The results of the TG analysis indicate that the synthesized compound shows no mass loss in this temperature range. From the DSC curve (also in Fig. 3a and 3b), an endothermic peak at 378.2 K (with an "onset" at 362.6 K) during the heating stage with an enthalpy of 0.163 J/g (0.107 kJmol^{-1}) and an exothermic peak at 368.6 K (with an "onset" at 376.4 K) in the cooling with an enthalpy of 0.156 J/g (0.102 kJmol^{-1}) were estimated. Such a cycle thus exhibits a thermal hysteresis of 9.6 K between the two peaks (of 13.8 K from the onset temperatures), in addition to the similarity of the enthalpies, which is indicative of a phase transition with few structural changes. These low enthalpy values have been observed in other members of the $RE_2(MoO_4)_3$ (RE ≡ Pr–Ho) family of molybdates that are improper ferroelectrics [60,61]. The temperature of the ferroelectric-paraelectric transition is similar to that of holmium molybdate and lower than the other rare earth molybdates, as it is expected (smaller ionic radius [62]). We took advantage of this result to program thermodiffraction measurements to study the thermal evolution of the crystal structure before and after the phase transition.

3.3. Structural characterization and phase transition mechanisms

3.3.1. Thermal dependence of diffraction peaks, cell parameters and "amplimodes"

The Rietveld refinements of the β and β′ phases are plotted in Figs. 4 and 5, respectively. A slight shift of the diffraction peaks to smaller angles is generally detected, commensurate with an increase in the unit cell volume. The excellent agreement between the observed and calculated
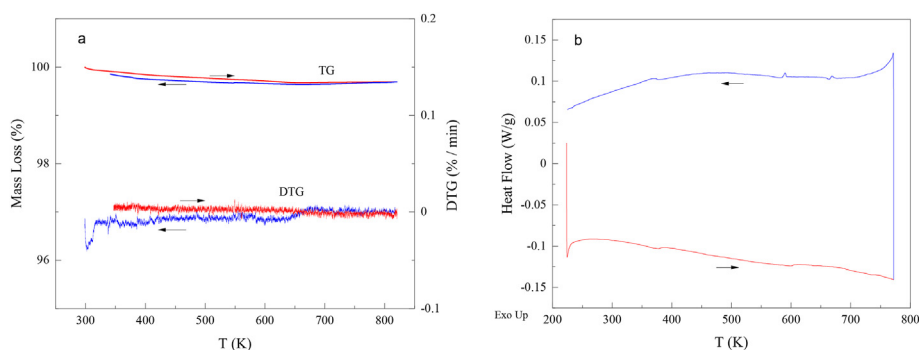

Fig. 2. TG-DTG (a) and DSC (b) curves for heating (red) - cooling (blue) cycle taken at the rate of 10 K/min for the $Y_2(MoO_4)_3$ sample.
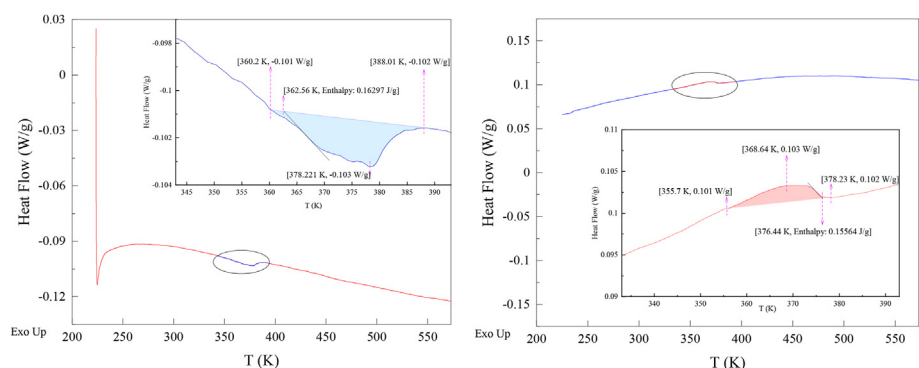

Fig. 3. DSC curve during the heating stage (223 K → 600 K) on the left and the cooling stage (600 K → 223 K) on the right. The inset graph zooms both curves highlighting the phase transition in the interval [343, 393 K].
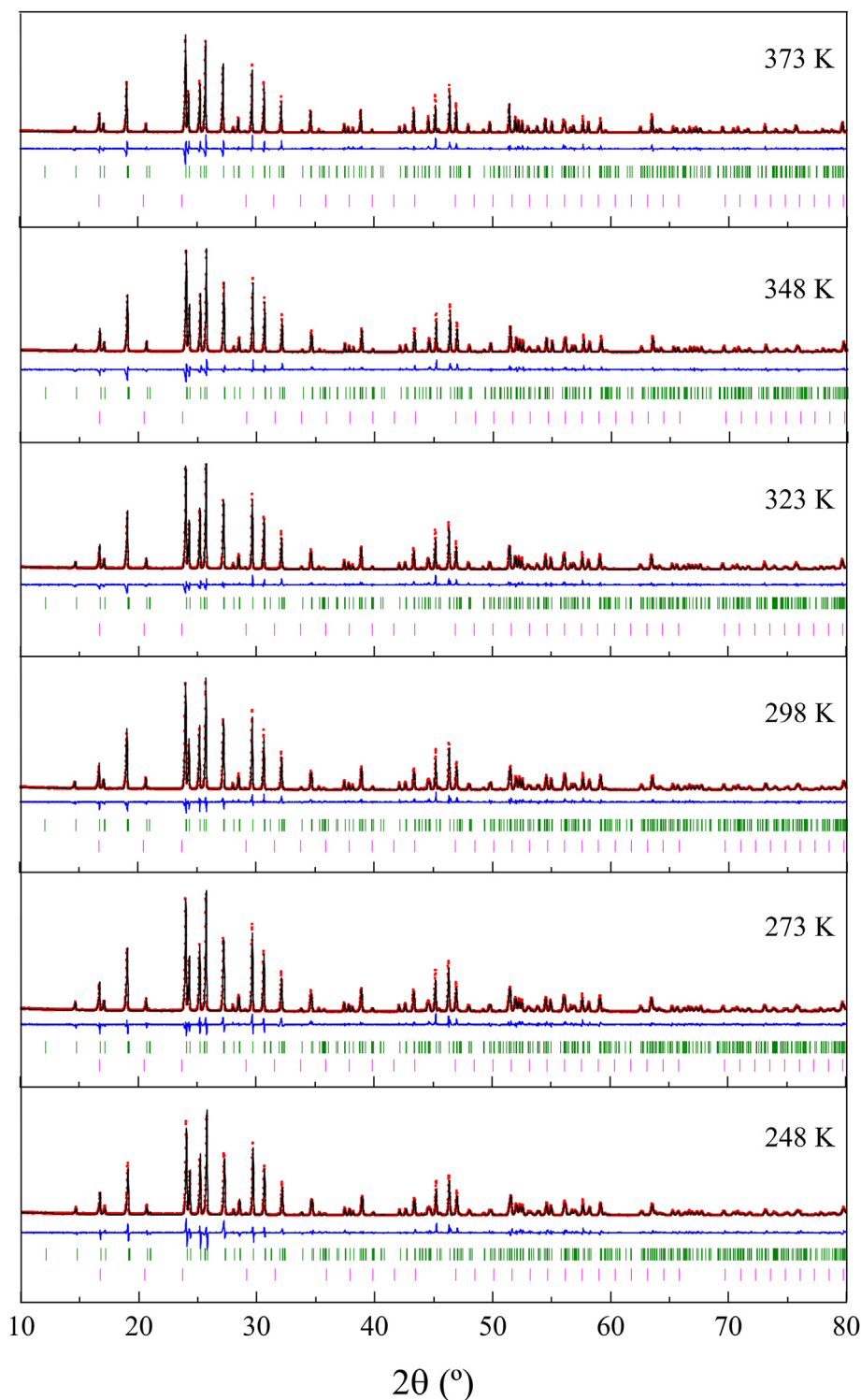
Fig. 4. Rietveld refinement of the ferroelectric phase of $Y_2(MoO_4)_3$ at different temperatures: 248, 273, 298, 323, 348 and 373 K. Experimental observed data (red) and calculated data (black), the difference between observed and calculated data (blue) are indicated. The Bragg positions for each of the phases: β'-$Y_2(MoO_4)_3$ (green) and Y_2O_3 (pink) are also noted.

values is observed. The results of the Le Bail refinement performed with the diffractograms taken at high temperatures were also outstanding. Tables 2–4 show the lattice parameters, reliability factors, fractional coordinates, and isotropic thermal displacements of the β- and β′-phases at 373 K, refined by conventional and using "amplimodes" as it has been explained in section 2.4.1. Note that some coordinates have no standard deviation because the "amplimodes" that contribute to calculating the

distance of the atoms from the prototype phase have been nullified since they are very short (less than thermal displacements). Maximum and minimum values of the reliability factors for refinements at all temperatures are shown in Table A1 (supplementary material), which can be comparable to those obtained in the Rietveld refinement of the non-hydrated γ-phase [31,63].

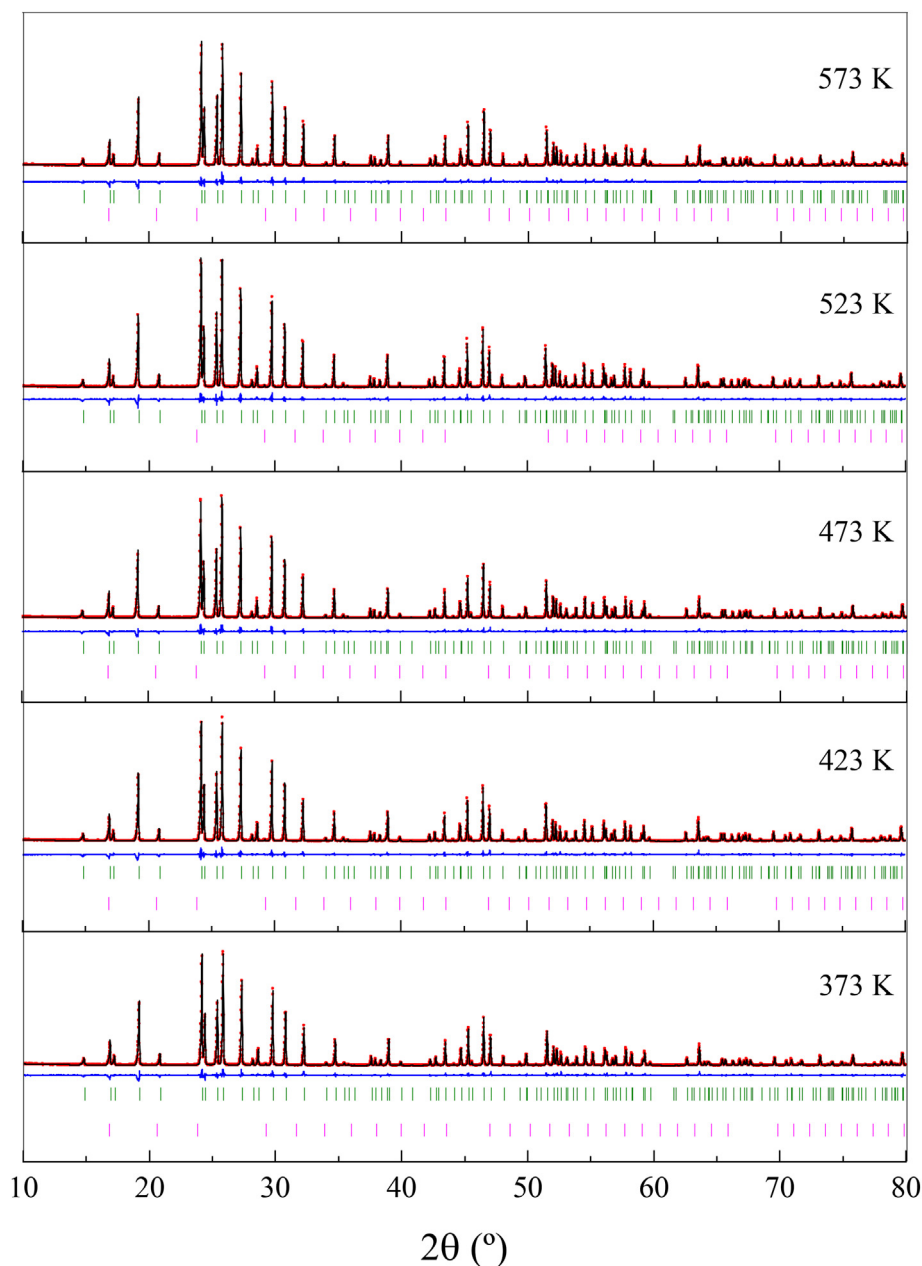In Fig. 6a, we plot the values of the cell parameters calculated with

Fig. 5. Rietveld refinement of the ferroelectric phase of $Y_2(MoO_4)_3$ at different temperatures: 373, 423, 473, 523 and 573 K. Experimental observed data (red) and calculated data (black), the difference between observed and calculated data (blue) are indicated. The Bragg positions for each of the phases: β'-$Y_2(MoO_4)_3$ (green) and Y_2O_3 (pink) are also noted.

Table 2

Cell parameters, "amplimodes" and agreement factors were obtained in the refinement of the diffractograms of the β- and β'-$Y_2(MoO_4)_3$ phases at 373 K.

	β -$Y_2(MoO_4)_3$	β'-$Y_2(MoO_4)_3$
a (Å)	7.31903(2)	10.34815(5)
b (Å)	7.31903(2)	10.33168(5)
c(Å)	10.56074(3)	10.56662(4)
V(Å³)	565.719(3)	1175.61(2)
Γ_1 (Å)	0.11(2)	0.41(2)
Γ_3 (Å)	0	0.25(6)
M_2+M_4 (Å)	0	1.21(4)
R_p/R_{wp} (%)	9.56/12.7	11.9/12.6
R_{exp} (%)	8.58	6.92
$\chi2$	2.18	3.32
R_B/R_F (%)	3.60/2.52	6.73/4.57

both refinements. The evolution of lattice parameters with temperature is very similar to that obtained for the holmium molybdate [40] and very recently for the gadolinium molybdate [64]. Parameters *a* and *b* grow with increasing temperature and equalize upon reaching the transition temperature, while parameter *c* decreases until reaching this temperature, then grows very slowly. It is detected that the transition temperature is around 378 K, as expected from the thermal analysis results (see Fig. 3).

In Fig. 6b, the amplitudes of the displacements from the paraelectric phase (at 373 K) for both the paraelectric and ferroelectric phases are plotted, with the symmetry of the Γ_1 modes in both cases and the M_2+M_4, and the Γ_3 for the ferroelectric phase. As expected [51], the primary nonpolar M_2+M_4 mode of higher amplitude than the secondary polar Γ_3 mode with an amplitude similar to that of the Γ_1 mode of the ferroelectric phase is distinguished. The values obtained are the same order of magnitude as those calculated for other compounds with the

Table 3
Fractional coordinates X, Y, Z (Å) and B_{iso} (Å^2) for the β and β' phases of $Y_2(MoO_4)_3$ at 373 K calculated as it is explained in section 2.3.

		β -$Y_2(MoO_4)_3$			B_{iso}	β'-$Y_2(MoO_4)_3$				B_{iso}
		X(Å)	Y(Å)	Z(Å)			Y(Å)	Z(Å)	X(Å)	
Y(1)	4e	0.3139(1)	0.8139(1)	0.2622(1)		4c	0.0044(4)	0.31350	0.26210	1.03(9)
Y(12)						4c	0.81350	−0.0044(4)	0.73790	0.86(8)
Mo(1)	2a	0.000000	0.000000	0.000000		4c	0.2461(4)	0.7539(4)	0.00000	1.21(4)
Mo(2)	4e	0.2941(1)	0.7941(1)	0.6429(1)		4c	0.0055(5)	0.29410	0.64270	1.14(8)
Mo(22)						4c	0.79410	0.00000	0.35730	1.10(8)
O(1)	4e	0.04270	0.19000	0.9038(6)	2.0(2)	4c	0.163(1)	0.876(1)	0.9047(5)	2.1(2)
O(12)						4c	0.315(1)	0.646(1)	0.9047(5)	2.1(2)
O(2)	4e	0.2723(9)	0.5011(1)	0.3000(6)	3.4(2)	4c	0.3650(4)	0.8260(4)	0.0953(5)	2.1(2)
O(22)						4c	0.1350(4)	0.6740(4)	0.0953(5)	2.1(2)
O(3)	4e	0.30630	0.80630	0.47930	3.0(2)	4c	0.130(2)	0.119(2)	0.280(1)	2.3(2)
O(32)						4c	0.351(2)	0.346(2)	0.318(1)	2.3(2)
O(33)						4c	0.6292(1)	0.881(1)	0.707(2)	2.3(2)
O(34)						4c	0.8435(1)	0.647(1)	0.696(2)	2.3(2)
O(4)	4e	0.12820	0.62820	0.69140	1.1(2)	4c	0.00000	0.311(2)	0.47861	2.5(2)
O(42)						4c	0.800(2)	−0.021(3)	0.52139	2.5(2)
O(43)						4c	0.00000	0.12599	0.69145	1.3(2)
O1(44)						4c	0.62599	0.00000	0.30855	1.3(2)

Table 4
Anisotropic atomic displacement x10^{-4} (Å^2) for the β-phase of $Y_2(MoO_4)_3$ at 373 K.

	β -$Y_2(MoO_4)_3$					
	β_{11}	β_{22}	β_{33}	β_{12}	β_{13}	β_{23}
Y(1)	51(2)	51(2)	19(2)	−9(3)	−2(1)	−2(3)
Mo(1)	62(3)	62(3)	16(2)	0	0	0
Mo(2)	51(2)	51(2)	23(2)	−13(3)	3(1)	3(1)

β'-$Gd_2(MoO_4)_3$ phase [51,65,66]. Regarding the crystal structure (atomic coordinates shown in Table 2), important changes were not observed related to those published in Refs. [7,28].

3.3.2. Structural mechanisms of the phase transition

Since phase transition mechanisms are investigates, it is necessary to discuss the thermal evolution of the crystal structure. Tables A2, A3 and A4 (supplementary material) show the absolute atom distances from the prototype phase, corresponding to every irreducible representation: Γ_1, Γ_3 and M_2+M_4, respectively, as information reference. The crystal structure of the ferroelectric phase at room temperature is presented in Fig. 7. The oxygen atoms have been labeled to facilitate the discussion.

In Figs. 8 and 9, the bond distances of tetrahedra and polyhedra from 248 K to 573 K are plotted. There are three independent MoO$_4$ tetrahedra and two YO$_7$ coordination polyhedra for the ferroelectric phase while there are two tetrahedra and one coordination polyhedra for the paraelectric one. Generally, the refinement results for polycrystalline samples present higher dispersion and standard deviation than those obtained

with single crystals [7,67]. In the ferroelectric phase, these distances are more dispersed and have more significant standard deviations than for the paraelectric phase, with fewer parameters to refine due to the constraints imposed by the more symmetric space group and fewer atoms per unit cell. The Mo⋯O bond distances remain nearly constant with increasing temperature. Thus, the tetrahedra are quite regular and possible dispersions do not respond to a clear temperature-dependent pattern. This rigidity of the MoO_4^{-2} tetrahedra has recently been described in the ferroelectric-paraelectric transition of the $Gd_2(MoO_4)_3$ compound without refining the oxygen atoms [64].

The average Y⋯O bonds tend to increase slightly with the temperature. The coordination polyhedra of Y atoms maintain the coordination number seven and the "capsulated" triangular prism geometry [26]. We can underline the more chaotic behavior of the O(1), O(12), O(2) and O(22) oxygen atoms before the phase transition; these are located at Wyckoff positions in the paraelectric phase, so the greater freedom of movement in the ferroelectric phase does not allow us to see their thermal dependence more clearly.

By representing the evolution of the crystal structure at different temperatures, we can appreciate how these coordination environments are affected by the calculated displacements of the oxygen atoms compared to the prototype crystal structure. In Fig. 10, different views of these structures are presented where the three types of molybdate tetrahedra are placed without sharing vertices in three different layers [64] perpendicular to the *c*-axis. Between these layers, the Y atoms are placed, forming coordination polyhedra by sharing the vertices of the tetrahedra. The black, red and blue arrows indicate the displacements of the oxygens from the prototype (paraelectric) structure with the
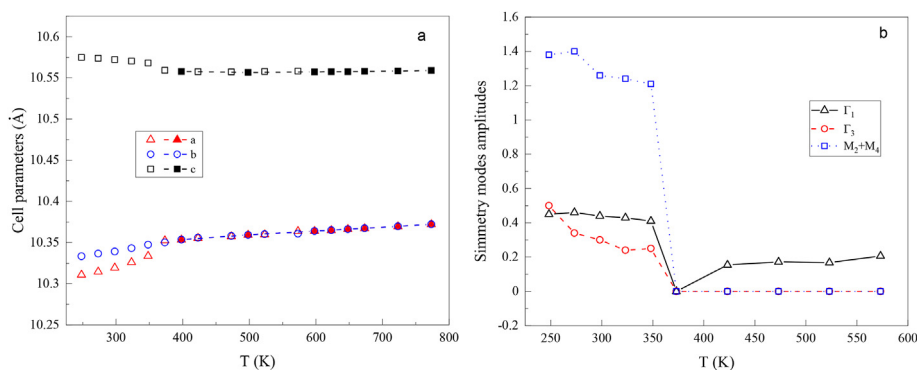

Fig. 6. (a) Cell parameters of $Y_2(MoO_4)_3$ as a function of temperature. (b) Amplitudes of the global displacements, associated with the different symmetry modes, obtained by comparing with the prototype phase (β phase at 373 K).
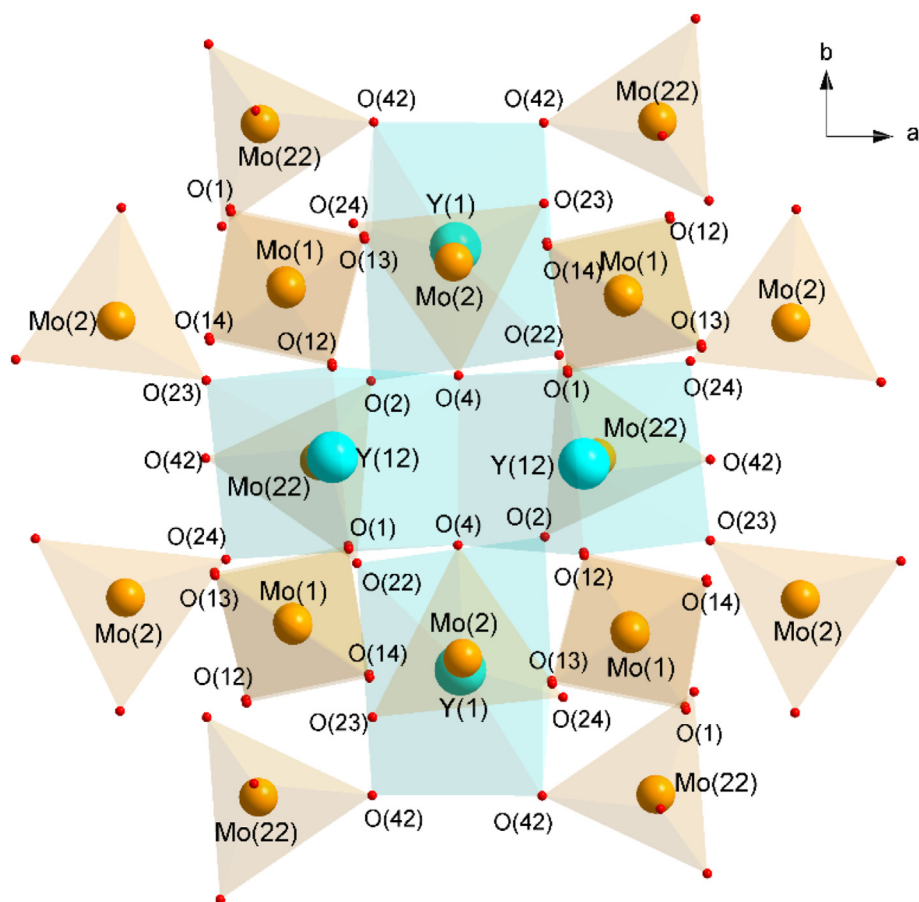
Fig. 7. Crystal structure of the β′-$Y_2(MoO_4)_3$ phase where the three symmetrically independent tetrahedra around Mo(1), Mo(2) and Mo(22) atoms and the two coordination environments corresponding to the Y(1) and Y(12) atoms are distinguished in pale orange and blue, respectively.

symmetry of Γ_1, Γ_3 and M_2+M_4 modes, respectively. Note that the amplitudes (moduli of the vectors) have been lengthened to visualize them better, each mode type having its scale. The displacements with Γ_1 mode symmetry are pictured in a projection perpendicular to the *c*-axis; with the naked eye, it can be seen that these displacements are, in general, longer at lower temperatures in the ferroelectric phase than at higher temperatures in the paraelectric phase. At the paraelectric phase (below), these displacements rotate the tetrahedra centered on Mo(1), while in the ferroelectric-ferroelastic phase, they tend to compress it (also occurs in other ferroelastic-paraelastic compounds [68,69]). The small displacements correspond to the O(2), O(22), O(23) and O(24) oxygen atoms from the Mo(2)- and Mo(22)-centered tetrahedra change their orientation with temperature. Still, they remain more or less constant in length. The displacements corresponding to the M_2+M_4 mode, viewed through the *b*-axis, are very similar and its orientation is not practically changed with the temperature. This primary mode, with a characteristic and well-defined thermal behavior, plays the leading role in the phase transition [51]. The shifts corresponding to the polar Γ_3 mode, viewed through the *b*-axis, have a more chaotic behavior, as in other ferroelectrics studied with this formalism [65]. The displacements of the O(4) and O(42) oxygen atoms have the more significant component in the *c*-axis and vary the most with temperature, both in their length and orientation. As the temperature decreases, these bonds disperse more clearly than the remaining bonds. These oxygen atoms form the most extended bonds in the tetrahedra, centered on the molybdenum atoms Mo(2) and Mo(22), and of both polyhedra centered on Y(1) and Y(12)(forming the common edge between the yttrium polyhedra). In addition, these oxygens atoms make up the Mo(22)···O(4)···Y(1) and Mo(2)···O(42)···Y(12) bridges so that when the Mo···O bond contracts, the corresponding Y···O bond expands. The arrangement of these shifts is very similar to that calculated

for the $La_{2-x}Er_x(MoO_4)_3$ series of compounds [66]. Many authors agree on the important role of these oxygen atoms in the formation of the ferroelectric phase [70].

In order to correlate these results with later results obtained by measuring macroscopic properties, we have to emphasize that it is not straightforward to calculate the spontaneous polarization from point charges because obtaining the positions of the oxygens and their effective charges is complicated. However, given the global displacement Γ_3 within the unit cell (with volume V_{cell}) and the electron charge *e*, the spontaneous polarization $P_s(\Gamma_3)$ can be estimated, obtaining values of the order of magnitude expected:

$$P_s(\Gamma_3) = e \cdot \Gamma_3 / V_{cell} \quad (4)$$

Values of P_s were obtained between 0.71 (at 248 K) and 0.35 (at 348 K) $\mu C/cm^2$, similar to those of other improper ferroelectrics. Note that the charge's value (in Eq. (4) the electron charge) is important in this calculation [71].

3.4. Dielectric and ferroelectric characterization. Crystal structure and properties correlations

3.4.1. Ferroelectric properties

The characterization carried out by differential scanning calorimetry and X-ray diffraction seems to indicate that yttrium molybdate, synthesized by solid state reaction, presents the characteristics of a ferroelectric material with a Curie temperature in the vicinity of 378 K. To confirm and characterize this ferroelectric behavior, hysteresis cycles have been carried out at room temperature (293 K) for different electric fields and a frequency of 2 Hz (Fig. 11a) and hysteresis cycles as a function of
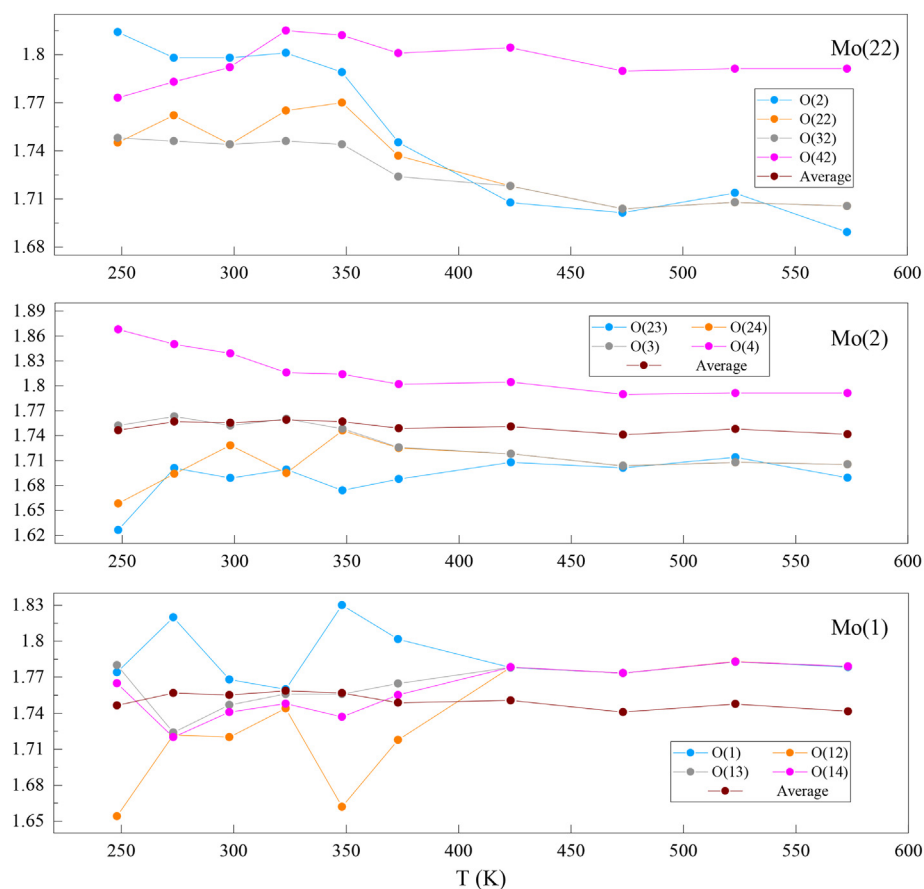
Fig. 8. Bond evolution of the tetrahedral environments of Mo(1), Mo(2) and Mo(22) for both phases of $Y_2(MoO_4)_3$. In addition to the evolution of the average Mo···O bond.

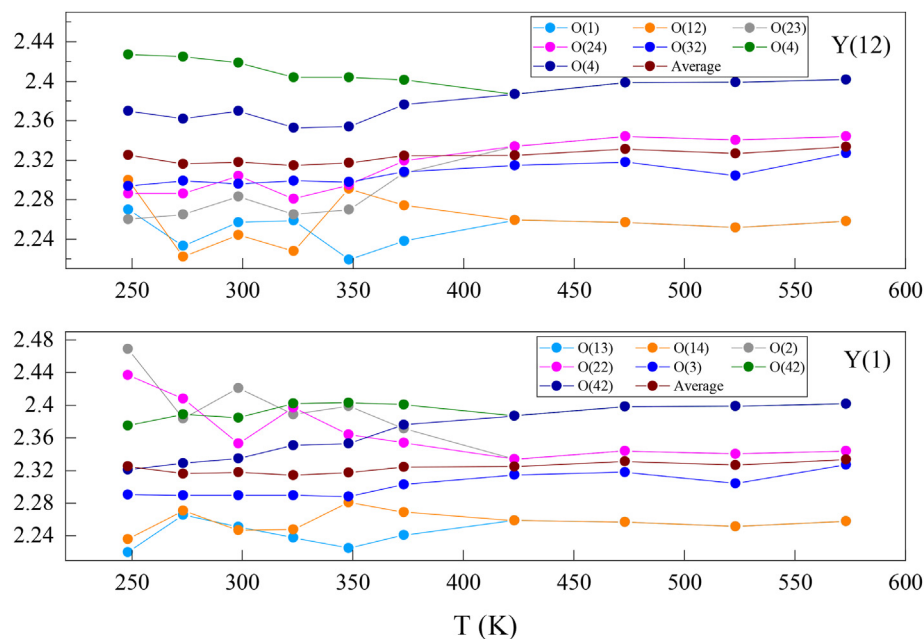**Fig. 9.** Bond evolution of the tetrahedral environments of Y(1) and Y(12), in addition to the evolution of the average Y···O bond for both phases of $Y_2(MoO_4)_3$.

temperature under an applied electric field of 32.7 kV/cm at a frequency of 2 Hz (Fig. 11b). As shown in Fig. 11a, with the increase of the electric field, the area enclosed by each hysteresis cycle increases and therefore its features: the remaining polarization P_r, maximum polarization P_{max},

and coercive field E_c. The variation of the remanent polarization, coercive field, and area of the hysteresis cycle with the temperature at different applied electric fields is shown in Fig. A1 (supplementary material). The shape of the unsaturated loop, which is usually associated
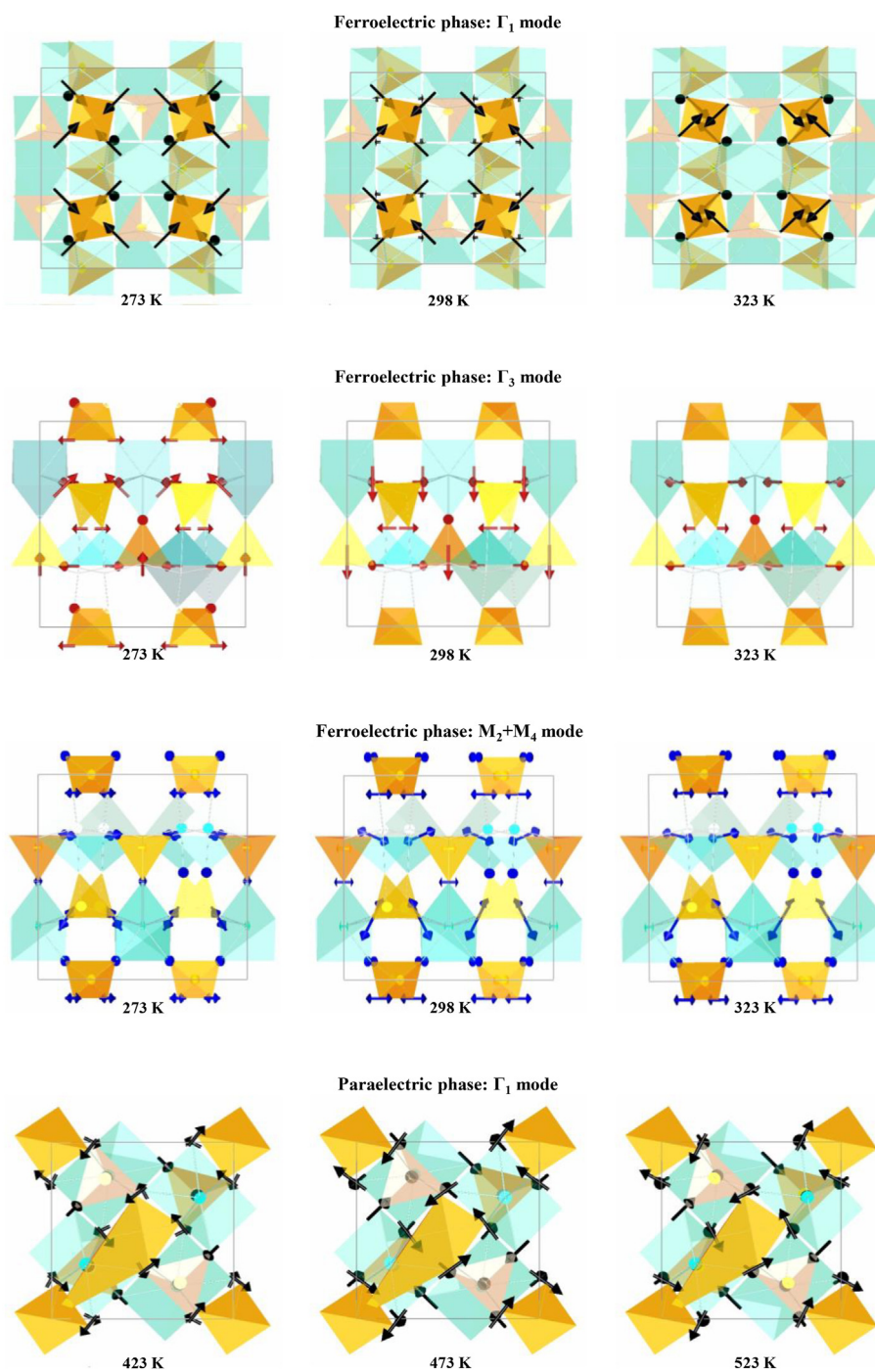
Fig. 10. Visualization of the "amplimodes" for of the β′ phase of $Y_2(MoO_4)_3$ with symmetries Γ_1 (view perpendicular to the *c*-axis), Γ_3 and M_2+M_4 (view perpendicular to the *b*-axis) and of the β phase with symmetry Γ_1 (view perpendicular to the *c*-axis). The arrows refer to the displacements of the oxygen atoms with the different symmetries from the prototype β-phase.

with leakage current losses in proper ferroelectrics [72], could have another origin in the improper ones since the primary structural order parameter (other than spontaneous polarization, which is the secondary) controls the switching dynamics [73]. In any case, the leakage currents losses may be present. They will slightly affect the existing hysteresis loop due to the relatively low density of the pellet, where the porosity hinders the movement of dipoles within the material (see Fig. 6) and contributes to electrical losses [74].

In Fig. 11b, it is observed that in the region where the material has a ferroelectric behavior, that is, according to DSC measurements, at temperatures below 378 K (Fig. 3) and, according to thermodiffraction at

temperatures below 373 K, it describes a hysteresis cycle whose area, remanent and maximum polarization and coercive field decreases with increasing temperature, without reaching the paraelectric phase due to equipment limitations. The decrease in the cycle area and its parameters confirms the ferroelectric-paraelectric transition.

Moreover, the maximum and remanent polarization values agree qualitatively with the structural results, where the ferroelectric distortion also decreases, generally, with lowering the temperature. A decrease in the amplitude of the mode Γ_3 is observed with increasing temperature. In the previous section, we have estimated the spontaneous polarization from the displacements compatible with this symmetry mode, and it can
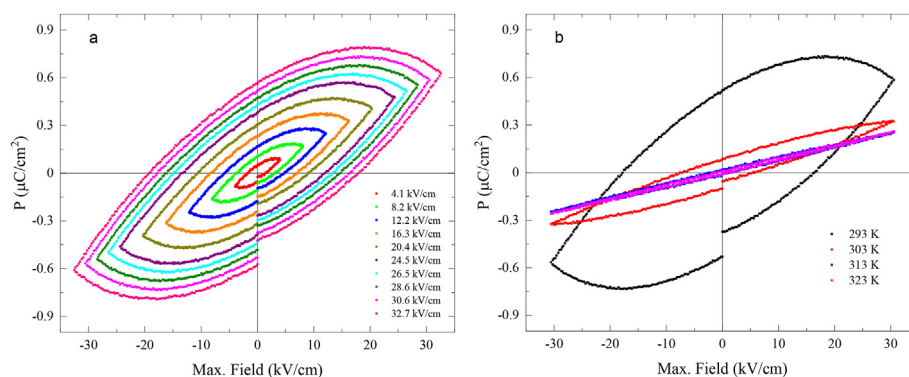
Fig. 11. (a) Hysteresis cycle at room temperature (293 K) at 2 Hz, under the application of different electric fields for a sintered $Y_2(MoO_4)_3$ pellet. (b) Hysteresis cycles at different temperatures under an electric field of 32.7 kV/cm and 2 Hz for the same pellet.
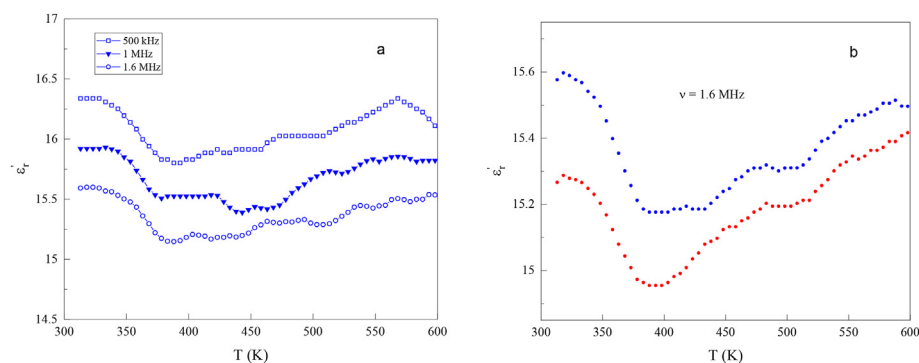

Fig. 12. (a) Real part of the complex dielectric permittivity as a function of temperature at 500 kHz (□), 1 MHz (▼) and 1.6 MHz (○), during the cooling stage, for a $Y_2(MoO_4)_3$ pellet. (b) Real part of the complex dielectric permittivity as a function of temperature at 1.6 MHz during the heating (red) - cooling (blue) cycle for the same pellet.

be seen that these are values of the same order of magnitude as the polarizations obtained from the hysteresis cycle. Comparing these results with those obtained for the $La_{1.25}Er_{0.75}(MoO_4)_3$ compound [66], we found a similar amplitude of the Γ_3 symmetry mode.

On the other hand, similar unsaturated cycles and values of P_s, P_m (applying similar electric fields, at room temperature) are also observed in the above solid solution and single crystals of β'-$Tb_2(MoO_4)_3$ (well-known improper ferroelectric) [75]. It is more difficult to develop leakage currents for single crystals than for powder samples with low densification. It can also be seen in terbium molybdate how the loop area, P_m and P_r decrease with increasing temperature, and saturation is reached more quickly. It is the case of yttrium molybdate at 303 K with a slightly more saturated cycle than that obtained at 293 K (Fig. 11b). Then, we can consider the appearance of the cycles to confirm that we are dealing with a ferroelectric material; the observed anomalies indicate a key role of the primary order parameter (with the symmetry of the irreducible representation M_2+M_4) on the energetics of the polarization switching. Finally, given the lack of a detailed understanding of the polarization dynamics in improper ferroelectrics, possibly because there are fewer exemplars [73], comprehensive studies (including the visualization and the analysis of hysteresis loops) in other families of improper ferroelectrics are necessary.

3.4.2. Thermal dependence of the dielectric properties

In Fig. 12, the dependence of the real part of the relative complex dielectric permittivity (ε_r') on the temperature at three frequencies (500 kHz, 1 MHz, and 1.6 MHz), during the cooling (Fig. 12a) and heating (Fig. 12b) stages for a yttrium molybdate pellet is shown. It is observed that ε_r' present its minimum value in the vicinity of 383 K for all three frequencies and then increases again with increasing temperature. The

temperature at which the dielectric anomaly is observed (383 K) is very close to the transition temperature detected by DSC measurements (378.2 K). The value of ε_r' ranges from 15 to 16; thus, for a frequency of 500 MHz, it varies from 16.1 (313 K) to 15.7 (383 K) and then takes a value of 15.9 at 600 K. This weak anomaly of ε_r' in the vicinity of the transition temperature, compatible with the observed minor transition enthalpy and small structural changes, is characteristic of improper ferroelectrics. These anomalies are more pronounced in isostructural compounds with higher transition temperatures and more energetic transitions [66]. The dielectric permittivity measurements also informed about new irregularities at a higher temperature before the expected transition to the γ-phase, around 660 K [41]. The scattering of the real part of the electrical permittivity leads to changes in the analyzed electrical conductivity.

Fig. 13 presents the results of the real part of the electrical conductivity ($\sigma'(\omega)$) as a function of frequency and temperature for both stages. It is observed that the conductivity increases with temperature for a fixed frequency, and the conductivity's dependence on frequency is more significant as it increases with temperature; therefore, the Universal Dielectric response model and the corresponding fit (Eq. (3)) have been used. From these adjustments, the thermal dependence of the s parameter (Fig. 14a) and the electrical conductivity (σ_{dc}), which ranges between 10^{-9} and 10^{-5} S/cm (Fig. 14b), have been obtained in the heating and cooling stages. The evolution of the s parameter shows that the material's behavior is similar in both stages, with a small anomaly around 433 K during the heating process, and between 513 and 573 K during the cooling process. Beyond that, there is a progressive decrease up to about 875 K for both stages, indicating an upcoming phase transition.

Furthermore, the dependence of the conductivity, represented as $\ln(\sigma_{dc})$ versus 1000/T (Fig. 14b), allows the differentiation between
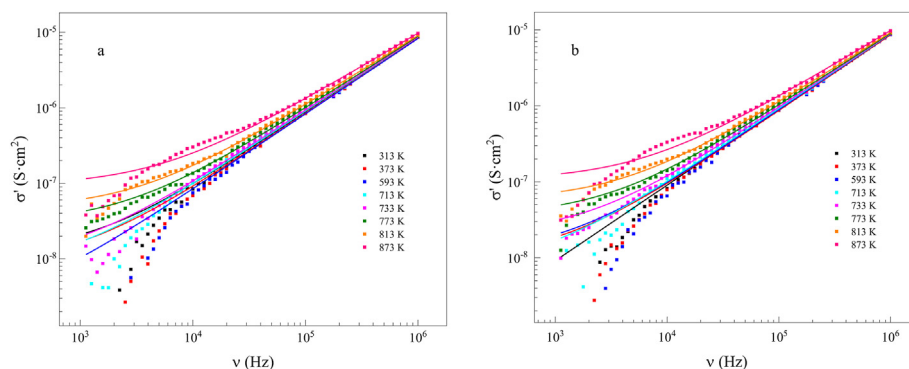
Fig. 13. Real part of the electrical conductivity as a function of frequency at various temperatures during the heating (a) and cooling (b) stage for a sintered $Y_2(MoO_4)_3$ pellet. The solid lines correspond to the fits to equation (3).
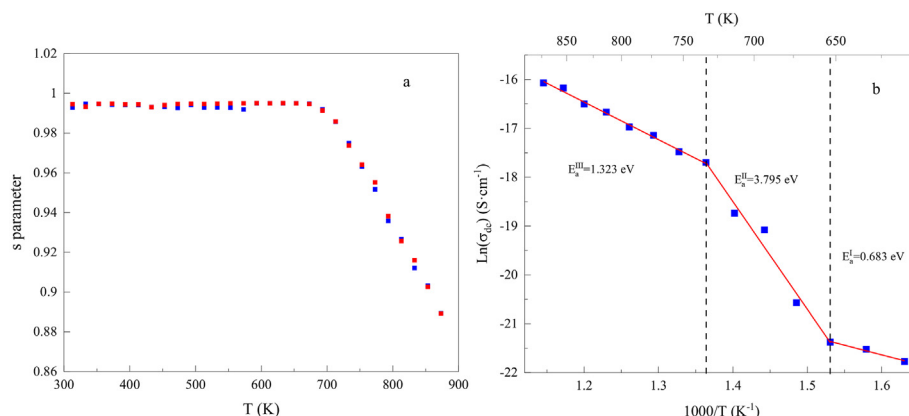

Fig. 14. Results of complex conductivity fitting measured on $Y_2(MoO_4)_3$ pellets. (a) Parameter s for the heating (red) and cooling (blue) stages. (b) Ahrrenius-plot of σ_{dc} indicating the three regions with different activation mechanisms for the cooling stage.

three regions with respective activation energies during the activation process. The values of the activation energies were calculated by fitting with equation (4). They were 1.323 ± 0.232 eV and 3.795 ± 1.950 eV for temperatures above 673 K and 0.683 ± 0.517 eV for temperatures above 634 K. The intermediate region stands out with a high value of the activation energy compared to that obtained for the other two regions. These changes in conductivity have also been detected in α-RE$_2$(MoO$_4$)$_3$ molybdates within the modulated scheelite family [Sm$_2$(MoO$_4$)$_3$ and Eu$_2$(MoO$_4$)$_3$] [59,76] and were associated with changes in the electronic-polaronic-ionic conductivity mechanisms that were correlated with small changes in the crystal structure resulting in a strange behavior in the a parameter. In the case of the yttrium molybdate, we plotted (Fig. 15) the natural logarithm evolution of the lattice parameters versus 1000/T before the β-γ phase transition to better highlight the correlation between the electrical and the structural parameters. Three regions can also be distinguished due to the anomalous behavior of the c parameter. It would be necessary to perform measurements at more temperatures, both dielectric and diffraction to be able to arrive at results that explain these thermal effects.

4. Conclusions

Polycrystals of the β'-Y$_2$(MoO$_4$)$_3$ phase have been synthesized with high purity. The experimental conditions have been explained in detail so they can be reproduced. X-ray diffraction patterns have been identified and refined with the ferroelectric-ferroelastic structure of the β'-Gd$_2$(MoO$_4$)$_3$ type, using the Rietveld method and refining the so-called "amplimodes" or displacements from the paraelectric-paraelastic (β-phase) compatibles with three symmetry modes (Γ_1, Γ_3 and
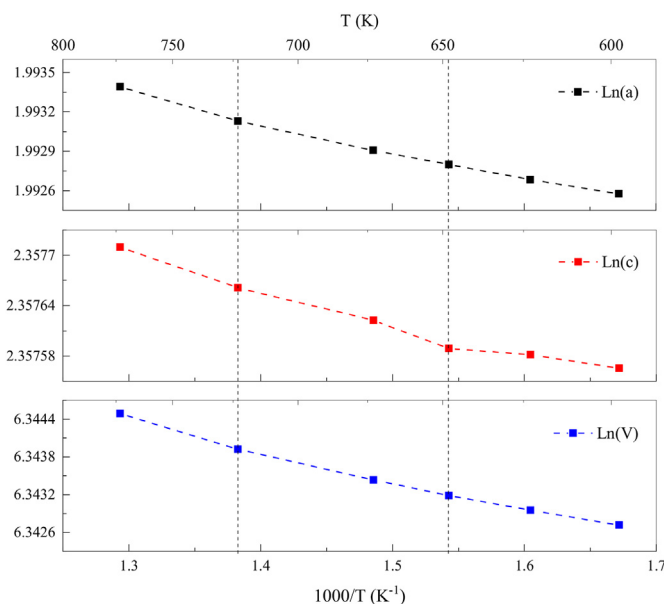

Fig. 15. Evolution of the cell parameters as $\ln[c(1000/T)]$, $\ln[a(1000/T)]$ and volume as $\ln[V(1000/T)]$ of the β-Y$_2$(MoO$_4$)$_3$ phase, where the three regions with different conductivity mechanisms at high temperature can be distinguished.

$M_2 + M_4$), instead of the atomic coordinates.

The Curie temperature has been determined between 373 and 383 K

from thermal analysis and dielectric spectroscopy in heating and cooling cycles. It has also been found that the crystalline structure at 348 K is still ferroelectric; at 398 K, it already belongs to the paraelectric phase. When comparing the ferroelectric hysteresis cycles at various temperatures, above room temperature, a clear decrease of the cycle area (and the maximum and remanent polarization) is observed, confirming the ferroelectric character of this compound. From the thermal dependence of the crystalline structure, it is confirmed to be an improper ferroelectric being the primary order parameter with the non-polar M_2+M_4 symmetry, as the highest displacement from the paraelectric phase. From the evolution of the polar mode Γ_3 (secondary order parameter) and the bond distances, it could be explained which oxygen atoms play the crucial role in the phase transition. The improper ferroelectric character is also confirmed by: 1) the small transition enthalpy obtained from the DSC analysis, 2) the fact that the transition is not clearly distinguishable for the dielectric measurements, and 3) the hysteresis cycles, with small polarization values, difficult to saturate, and with values within orders of magnitude of the estimated Γ_3-mode amplitudes.

Moreover, a region is found between 600 and 877 K in which the σ_{dc} undergoes high activation energy relative to the other two consecutive regions. This anomaly must have a structural character because a correlation is found with the evolution of the c parameter.

Compounds with the β'-$Y_2(MoO_4)_3$ phase are, definitively, multiferroic and multifunctional crystalline matrices very appropriate to host the series of lanthanides of smaller ionic radius and trivalent transition metals, that have not been conveniently exploited. Moreover, it has the advantage that it is not a hydrated phase as is the case with the much more studied γ-phase.

CRediT authorship contribution statement

G. Gil-de-Cos: Conceptualization, Methodology, Visualization, Investigation, Supervision, Writing – review & editing. **M.E. Torres:** Conceptualization, Methodology, Visualization, Investigation, Supervision, Writing – review & editing. **C. González-Silgo:** Conceptualization, Methodology, Visualization, Investigation, Supervision, Writing – review & editing.

Declaration of competing interest

The authors declare that they have no known competing financial interests or personal relationships that could have appeared to influence the work reported in this paper.

Data availability

Data will be made available on request.

Appendix A. Supplementary data

Supplementary data to this article can be found online at https://doi.org/10.1016/j.jssc.2022.123738.

References

[1] A.M. Kaczmarek, R. Van Deun, Rare earth tungstate and molybdate compounds–from 0D to 3D architectures, Chem. Soc. Rev. 42 (23) (2013) 8835–8848, https://doi.org/10.1039/C3CS60166H.

[2] F. Lei, B. Yan, Hydrothermal synthesis and luminescence of $CaMO_4$: RE^{3+} (M = W, Mo; RE = Eu, Tb) submicro-phosphors, J. Solid State Chem. 181 (4) (2008) 855–862, https://doi.org/10.1016/j.jssc.2008.01.033.

[3] L. Macalik, Comparison of the spectroscopic and crystallographic data of Tm3+ in the different hosts: $KLn(MoO_4)_2$ where Ln = Y, La, Lu and M = Mo, W, J. Alloys Compd. 341 (1–2) (2002) 226–232, https://doi.org/10.1016/S0925-8388(02)00084-1.

[4] C.A. Kodaira, H.F. Brito, M.C.F. Felinto, Luminescence investigation of Eu3+ ion in the $RE_2(WO_4)_3$ matrix (RE = La and Gd) produced using the Pechini method, J. Solid State Chem. 171 (1–2) (2003) 401–407, https://doi.org/10.1016/S0022-4596(02)00221-9.

[5] Y. Zhou, X.H. He, B. Yan, Self-assembled $RE_2(MoO_4)_3$: ln^{3+} (RE = Y, La, Gd, Lu; M = W, Mo; Ln = Yb/Er, Yb/Tm) hierarchical microcrystals: hydrothermal synthesis and up-conversion luminescence, Opt. Mater. 36 (3) (2014) 602–607, https://doi.org/10.1016/j.optmat.2013.10.036.

[6] P. Kumar, B.K. Gupta, New insight into rare-earth doped gadolinium molybdate nanophosphor assisted broad spectral converters from UV to NIR for silicon solar cells, RSC Adv. 5 (31) (2015) 24729–24736, https://doi.org/10.1039/C4RA15383A.

[7] S. Laufer, S. Strobel, T. Schleid, J. Cybinska, A.V. Mudring, I. Hartenbach, Yttrium (III) oxomolybdates (VI) as potential host materials for luminescence applications: an investigation of Eu^{3+}-doped $Y_2[MoO_4]_3$ and $Y_2[MoO_4]_2[Mo_2O_7]$, New J. Chem. 37 (7) (2013) 1919–1926, https://doi.org/10.1039/C3NJ00166K.

[8] A.G. Bispo Jr., G.M. Shinohara, A.M. Pires, C.X. Cardoso, Red phosphor based on Eu^{3+}-doped $Y_2(MoO_4)_3$ incorporated with Au NPs synthesized via Pechini's method, Opt. Mater. 84 (2018) 137–145, https://doi.org/10.1016/j.optmat.2018.06.023, 2018.

[9] M. Janulevicius, P. Marmokas, M. Misevicius, J. Grigorjevaite, L. Mikoliunaite, S. Sakirzanovas, A. Katelnikovas, Luminescence and luminescence quenching of highly efficient $Y_2Mo_4O_{15}$: Eu^{3+} phosphors and ceramics, Sci. Rep. 6 (1) (2016) 1–12, https://doi.org/10.1038/srep26098.

[10] Y. Tian, B. Chen, B. Tian, R. Hua, J. Sun, L. Cheng, Q. Meng, Concentration-dependent luminescence and energy transfer of flower-like $Y_2(MoO_4)_3$: Dy^{3+} phosphor, J. Alloys Compd. 509 (20) (2011) 6096–6101, https://doi.org/10.1016/j.jallcom.2011.03.034.

[11] Y. Zhou, B. Yan, $RE_2(MoO_4)_3$: ln^{3+} (RE = Y, La, Gd, Lu; M= W, Mo; Ln = Eu, Sm, Dy) microcrystals: controlled synthesis, microstructure and tunable luminescence, Crystal Engineering Communication 15 (2013) 5694–5702, https://doi.org/10.1039/C3CE40495A.

[12] H. Deng, Z. Zhao, J. Wang, Z. Hei, M. Li, H.M. Noh, R. Yu, Photoluminescence properties of a new orange–red emitting Sm^{3+}-doped $Y_2Mo_4O_{15}$ phosphor, J. Solid State Chem. 228 (2015) 110–116, https://doi.org/10.1016/j.jssc.2015.04.023.

[13] D. Hou, X. Pan, Li Jinyan, W. Zhou, Y. Xinyu, Structure and luminescence properties of Sm^{3+} doped Y_2MoO_6 phosphor under near ultraviolet light excitation, J. Rare Earths 35 (2017) 335–340, https://doi.org/10.1016/S1002-0721(17)60916-5.

[14] W. Lu, L. Cheng, J. Sun, H. Zhong, X. Li, Y. Tian, H. Yu, The concentration effect of upconversion luminescence properties in Er^{3+}/Yb^{3+}-codoped $Y_2(MoO_4)_3$ phosphors, Phys. B Condens. Matter 405 (2010) 3284–3288, https://doi.org/10.1016/j.physb.2010.04.061.

[15] M. Mondal, V.K. Rai, Ho^{3+}/Yb^{3+}: $YMoO_4$ core@ shell nanoparticles for enhanced visible upconversion and security applications, J. Alloys Compd. 750 (2018) 304–311, https://doi.org/10.1016/j.physb.2010.04.061.

[16] T. Wang, S. Wang, H. Zhang, X. Zou, Y. Wei, W. Hu, C. Su, C. Preparation, Luminescence properties and energy transfer of Tm^{3+} and Tm^{3+}-Eu^{3+} doped glass-ceramics containing $NaY(MoO_4)_2$, J. Solid State Chem. 284 (2020) 121184, https://doi.org/10.1016/j.jssc.2020.121184.

[17] S. Georges, F. Goutenoire, P. Lacorre, M.C. Steil, Sintering and electrical conductivity in fast oxide ion conductors $La_{2-x}R_xMo_{2-y}W_yO_9$ (R: Nd, Gd, Y), J. Eur. Ceram. Soc. 25 (2005) 3619–3627, https://doi.org/10.1016/j.jeurceramsoc.2004.09.029.

[18] N. Imanaka, Y. Kobayashi, K. Fujiwara, T. Asano, Y. Okazaki, G. Adachi, Trivalent rare earth ion conduction in the rare earth tungstates with the $Sc_2(WO_4)_3$-type structure, Chem. Mater. 10 (7) (1998) 2006–2012, https://doi.org/10.1021/cm980157e.

[19] C. Jiang, T. Liu, N. Peng, R. Zheng, J. Zhang, X. Cheng, J. Shu, Facile synthesis of $Y_2(MoO_4)_3$ nanowires as anode materials towards enhanced lithium storage performance, J. Electroanal. Chem. 841 (2019) 111–118, https://doi.org/10.1016/j.jelechem.2019.04.039.

[20] T.W. Chen, J.V. Kumar, S.M. Chen, B. Mutharani, R. Karthik, E.R. Nagarajan, V. Muthuraj, Rational construction of novel rose petals-like yttrium molybdate nanosheets: a janus catalyst for the detection and degradation of cardioselective β-blocker agent acebutolol, Chem. Eng. J. 359 (2019) 1472–1485, https://doi.org/10.1016/j.cej.2018.11.029.

[21] S.F. Solodovnikov, Z.A. Solodovnikova, E.S. Zolotova, V.N. Yudin, O.A. Gulyaeva, Y.L. Tushinova, B.M. Kuchumov, Nonstoichiometry in the systems

Na$_2$MoO$_4$–MMoO$_4$ (M= Co, Cd), crystal structures of Na$_{3.36}$Co$_{1.32}$(MoO$_4$)$_3$, Na$_{3.13}$Mn$_{1.43}$(MoO$_4$)$_3$ and Na$_{3.72}$Cd$_{1.14}$(MoO$_4$)$_3$, crystal chemistry, compositions and ionic conductivity of alluaudite-type double molybdates and tungstates, J. Solid State Chem. 253 (2017) 121–128, https://doi.org/10.1016/j.jssc.2017.05.031.

[22] V.G. Grossman, J.G. Bazarova, M.S. Molokeev, B.G. Bazarov, New triple molybdate K$_5$ScHf(MoO$_4$)$_6$: synthesis, properties, structure and phase equilibria in the M$_2$MoO$_4$–Sc$_2$(MoO$_4$)$_3$–Hf(MoO$_4$)$_2$ (M= Li, K) systems, J. Solid State Chem. 283 (2020), 121143, https://doi.org/10.1016/j.jssc.2019.121143.

[23] X. Cheng, Z. Wang, H. Zhang, Y. Ren, X. Zhu, K. Yang, Structural stability and phonon anharmonicity of Y$_2$MoO$_6$: Raman spectroscopic and XRD studies, Phys. B Condens. Matter 521 (2017) 43–48, https://doi.org/10.1016/j.physb.2017.04.020.

[24] M. Guzik M, E. Bieza, Y. Tomaszewicz, G. Guyot, G. Boulon, Chapter 17 research on the Yb^{3+} ion activated cubic molybdates and molybdato-tungstates for optical transparent ceramics, in: B. Di Bartolo, L. Silvestri, M. Cesaria, J. Collins (Eds.), Quantum Nano-Photonics. NATO 2017. NATO Science for Peace and Security Series B: Physics and Biophysics, Springer, Dordrecht, 2018, https://doi.org/10.1007/978-94-024-1544-5_17.

[25] J.S.O. Evans, T.A. Mary, A.W. Sleight, Negative thermal expansion in a large molybdate and tungstate family, J. Solid State Chem. 133 (2) (1997) 580–583, https://doi.org/10.1006/jssc.1997.7605.

[26] L.H. Brixner, J.R. Barkley, W. Jeitschko, Rare earth molybdates (VI), Handb. Phys. Chem. Rare Earths 3 (1979) 609–654, https://doi.org/10.1016/S0168-1273(79)03013-0.

[27] M. Maczka, A.G. Souza Filho, W. Paraguassu, P.T.C. Freire, J.M. Filho, J. Hanuza, Pressure-induced structural phase transitions and amorphization in selected molybdates and tungstates, Prog. Mater. Sci. 57 (2012) 1335–1385, https://doi.org/10.1016/j.pmatsci.2012.01.001.

[28] S.D. Gates, C. Lind, Polymorphism in yttrium molybdate Y$_2$Mo$_3$O$_{12}$, J. Solid State Chem. 180 (2007) 3510–3514, https://doi.org/10.1016/j.jssc.2007.10.011.

[29] J.S.O. Evans, T.A. Mary, A.W. Sleight, Negative thermal expansion in Sc$_2$(WO$_4$)$_3$, J. Solid State Chem. 137 (1) (1998) 148–160, https://doi.org/10.1006/jssc.1998.7744.

[30] B.A. Marinkovic, M. Ari, R.R. de Avillez, F. Rizzo, F.F. Ferreira, J.K. Miller, M.A. White, Correlation between AO$_6$ polyhedral distortion and negative thermal expansion in orthorhombic Y$_2$Mo$_3$O$_{12}$ and related materials, Chem. Mater. 21 (13) (2009) 2886–2894, https://doi.org/10.1021/cm900650c.

[31] C. Guzmán-Afonso, C. González-Silgo, J. González-Platas, M.E. Torres, A.D. Lozano-Gorrín, N. Sabalisck, V. Sánchez-Fajardo, J. Campo, J. Rodríguez-Carvajal, Structural investigation of the negative thermal expansion in yttrium and rare earth molybdates, J. Phys. Condens. Matter 23 (2011) 325402–325500, https://doi.org/10.1088/0953-8984/23/32/325402.

[32] A.W. Sleight, L.H. Brixner, A new ferroelastic transition in some A$_2$(MO$_4$)$_3$ molibdates and tungstates, J. Solid State Chem. 7 (2) (1973) 172–174, https://doi.org/10.1016/0022-4596(73)90152-7.

[33] S. Kojima, T. Nakamura, Electro-optical properties of gadolinium molybdate, Phys. Rev. B 18 (453) (1978), https://doi.org/10.1103/PhysRevB.18.453.

[34] T. Nakamura, E. Sawaguchi, Elastic and piezoelectric properties of Gd$_2$(MoO$_4$)$_3$, J. Phys. Soc. Jpn. 50 (1981) 2323–2328, https://doi.org/10.1143/JPSJ.50.2323.

[35] A.A. Kaminski, Orthorhombic ferroelectric and ferroelastic Gd$_2$(MoO$_4$)$_3$ crystal – a new many-purposed nonlinear and optical material: efficient multiple stimulated Raman scattering and CW and tunable second harmonic generation, Opt. Mater. 7 (1997) 59–73, https://doi.org/10.1016/S0925-3467(97)00006-2.

[36] H. Hao, H. Lu, R. Meng, Z. Nie, G. Ao, Y. Song, Y. Wang, X. Zhang, Thermometry via Au island-enhanced luminescence of Er^{3+}/Yb^{3+} Co-doped Gd$_2$(MoO$_4$)$_3$ thin films, J. Alloys Compd. 695 (2017) 2065–2071, https://doi.org/10.1016/j.jallcom.2016.11.045.

[37] E. Coy, P. Graczyk, L. Yate, K. Załęski, J. Gapiński, P. Kuświk, S. Mielcarek, F. Stobiecki, B. Mróz, C. Ferrater, S. Jurga, Second harmonic generation response in thermally reconstructed multiferroic β′-Gd$_2$(MoO$_4$)$_3$ thin films, Sci. Rep. 7 (2017) 1–9, https://doi.org/10.1038/s41598-017-12370-y.

[38] J. Nordlander, M. Campanini, M.D. Rossell, R. Erni, Q.N. Meier, A. Cano, N.A. Spaldin, M. Fiebig, M. Trassin, The ultrathin limit of improper ferroelectricity, Nat. Commun. 10 (2019) 5591, https://doi.org/10.1038/s41467-019-13474-x.

[39] L. Kuerten, S. Krohns, P. Schoenherr, K. Holeczek, E. Pomjakushina, T. Lottermoser, M. Trassin, D. Meier, M. Fiebig, Local control of improper ferroelectric domains in YMnO$_3$, Phys. Rev. B 102 (2020) 94108–94203, https://doi.org/10.1103/PhysRevB.102.094108.

[40] C. González-Silgo, C. Guzmán-Afonso, V.M. Sánchez-Fajardo, S. Acosta-Gutiérrez, A. Sánchez-Soares, M.E. Torres, N. Sabalisck, E. Matesanz, J. Rodríguez-Carvajal, Polymorphism in Ho$_2$(MoO$_4$)$_3$, Powder Diffr. 28 (2013) S33–S40, https://doi.org/10.1017/S0885715613001176.

[41] K. Nassau, J.W. Shiever, E.T. Keve, Structural and phase relationships among trivalent tungstates and molybdates, J. Solid State Chem. 3 (3) (1971) 411–419, https://doi.org/10.1016/0022-4596(71)90078-8.

[42] S. Sumithra, A.M. Umarji, Role of crystal structure on the thermal expansion of Ln$_2$W$_3$O$_{12}$ (Ln= La, Nd, Dy, Y, Er and Yb), Solid State Sci. 3 (2004) 1313–1319, https://doi.org/10.1016/j.solidstatesciences.2004.07.023.

[43] Universidad de La Laguna, Servicio general de Apoyo a la Investigación (SEGAI), servicio de Integrado de Difracción de Rayos X. https://www.ull.es/servicios/segai/servicios/difraccion-rx/.

[44] Universidad de La Laguna, Servicio general de Apoyo a la Investigación (SEGAI), servicio de Microscoía electrónica. https://www.ull.es/servicios/segai/servicios/microscopia-electronica/.

[45] Universidad de La Laguna, Servicio general de Apoyo a la Investigación (SEGAI). Servicio de Análisis térmico. https://www.ull.es/servicios/segai/servicios/analisis-termico/.

[46] Radiant Tecnologies, Inc.®, Radiant precisión series with visión software hardware architecture and system desing, Radiant Tecnologies, https://www.ferrodevices.com/1/297/lc.as, 2008.

[47] J. Rodríguez-Carvajal, Commission on powder diffraction (IUCr), Newsletter 26 (2001) 12–19. The complete program and documentation can be obtained in, http://journals.iucr.org/iucr-top/comm/cpd/Newsletters/, http://www.ill.eu/sites/fullprof/.

[48] E.N. Maslen, V.A. Streltsov, N. Ishizawa, A synchrotron X-ray study of the electron density in C-type rare earth oxides, Acta Crystallogr. Sect. B Struct. Sci. 52 (3) (1996) 414–422, https://doi.org/10.1107/S0108768195013371.

[49] D. Orobengoa, C. Capillas, M.I. Aroyo, J.M. Perez-Mato, AMPLIMODES: symmetry-mode analysis on the Bilbao crystallographic server, Journal of. Applied Crystallography 42 (2009) 820–833, https://doi.org/10.1107/S0021889809028064.

[50] J. Park, B.G. Kim, S. Mori, T. Oguchi, Tetrahedral tilting and ferroelectricity in Bi$_2$AO$_5$ (A = Si, Ge) from first principles calculations, J. Solid State Chem. 235 (2016) 68–75, https://doi.org/10.1016/j.jssc.2015.12.011.

[51] J.M. Perez-Mato, D. Orobengoa, M.I. Aroyo, Mode crystallography of distorted structures, Acta Crystallogr.: Foundations of Crystallography 66 (2010) 558–590, https://doi.org/10.1107/S0108767310016247.

[52] A. Le Bail, Whole powder pattern decomposition methods and applications: a retrospection, Powder Diffr. 20 (4) (2005) 316–326, https://doi.org/10.1154/1.2135315.

[53] D.A. Cardwell, D.S. Ginley, in: Handbook of Superconducting Materials: Superconductivity, Materials and Processes, first ed., CRC Press, Boca Raton, 2002 https://doi.org/10.1201/9781420034202.

[54] F.F. Lorraine, Materials Processing: A Unified Approach to Processing of Metals, Ceramics and Polymers, Prentice Hall, Englewood Cliffs, 1999, in: https://www.sciencedirect.com/book/9780123851321/materials-processing.

[55] A.K. Galwey, M.E. Brown, Thermal Decomposition of Ionic Solids, Elsevier, Amsterdam, 1999. https://www.sciencedirect.com/bookseries/studies-in-physical-and-theoretical-chemistry/vol/86/suppl/C.

[56] I. Bhat, S. Husain, W. Khan, S.I. Patil, Effect of Zn doping on structural, magnetic and dielectric properties of LaFeO$_3$ synthesized through sol–gel auto-combustion process, Mater. Res. Bull. 48 (2013) 4506–4512, https://doi.org/10.1016/j.materresbull.2013.07.028.

[57] S. Bdey, N.F. Bourguiba, S.N. Savvin, P. Nuñez, Na$_3$Bi(AsO$_4$)$_2$: synthesis, crystal structure and ionic conductivity, J. Solid State Chem. 272 (2019) 189–197, https://doi.org/10.1016/j.jssc.2019.01.034.

[58] A.K. Jonscher, Dielectric relaxation in solids, J. Phys. Appl. Phys. 32 (1999) R57, https://doi.org/10.1088/0022-3727/32/14/201.

[59] C. Guzmán-Afonso, M.E. Torres, C. González-Silgo, N. Sabalisck, J. González-Platas, E. Matesanz, A. Mujica, Electrical transport and anomalous structural behavior of α-Eu$_2$(MoO$_4$)$_3$ at high temperature, Solid State Commun. 151 (2011) 1654–1658, https://doi.org/10.1016/j.ssc.2011.08.009.

[60] M. Roy, R.N.P. Choudhary, H.N. Acharaya, Differential scanning calorimetric studies of ferroelectric rare-earth molybdates, Thermochim. Acta 145 (1989) 11–17, https://doi.org/10.1016/0040-6031(89)85122-6.

[61] Y. Tsukada, T. Honma, T. Komatsu, Self-powdering and nonlinear optical domain structures in ferroelastic β′-Gd$_2$(MoO$_4$)$_3$ crystals formed in glass, Journal of Solid Chemistry 182 (8) (2009) 2269–2273, https://doi.org/10.1016/j.jssc.2009.06.009.

[62] H.J. Borchardt, P.E. Bierstedt, Ferroelectric rare-earth molybdates, J. Appl. Phys. 38 (5) (1967) 2057–2060, https://doi.org/10.1063/1.1709828.

[63] B.A. Marinkovic, P.M. Jardim, R.R. de Avillez, F. Rizzo, Negative thermal expansion in Y$_2$Mo$_3$O$_{12}$, Solid State Sci. 7 (11) (2005) 1377–1383, https://doi.org/10.1016/j.solidstatesciences.2005.08.012.

[64] I.E. Nylund, M. Tsoutsouva, T. Grande, D. Meier, Observation of cation-specific critical behavior at the improper ferroelectric phase transition in Gd$_2$(MoO$_4$)$_3$, Physical Review Materials 6 (3) (2022), 034402, https://doi.org/10.1103/PhysRevMaterials.6.034402.

[65] C. Guzmán-Afonso, C. González-Silgo, M.E. Torres, N. Sabalisck, A.D. Lozano-Gorrín, J. González-Platas, E. Matesanz, Crystal structure and non-linear properties of A$_2$(MoO$_4$)$_3$ (A= Eu, Gd, Tb, Dy and Ho), Mater. Lett. 65 (17–18) (2011) 2731–2734, https://doi.org/10.1016/j.matlet.2011.05.075.

[66] G. Gil-de-Cos, M.E. Torres, C. González-Silgo, K. Soler-Carracedo, I.R. Martín, F. Rivera-López, S. Rodríguez-Rodríguez, Unexpected wide tuning of ferroelectric properties by varying the Er concentration in La2-xErx(MoO4)3 (x = 0.75, 1, 1.25) solid solutions, J. Solid State Chem. 315 (2022), 123462, https://doi.org/10.1016/j.jssc.2022.123462.

[67] S.C. Abrahams, C. Svensson, J.L. Bernstein, Ferroelectric–ferroelastic Tb$_2$(MoO$_4$)$_3$ crystal structure temperature dependence from 298 K through the transition at 436 K to the antiferroelectric–paraelastic phase at 523 K, J. Chem. Phys. 72 (8) (1980) 4278–4285, https://doi.org/10.1063/1.439720.

[68] W.I.F. David, A.M. Glazer, A.W. Hewat, The structure and ferroelastic phase transition of BiVO$_4$, Phase Transitions 1 (2) (1979) 155–169, https://doi.org/10.1080/01411597908213198.

[69] A.W. Sleight, L.H. Brixner, A new ferroelastic transition in some A$_2$(MO$_4$)$_3$ molibdates and tungstates, J. Solid State Chem. 7 (2) (1973) 172–174, https://doi.org/10.1016/0022-4596(73)90152-7.

[70] W. Jeitschko, A comprehensive X-ray study of the ferroelectric–ferroelastic and paraelectric–paraelastic phases of Gd$_2$(MoO$_4$)$_3$, Acta Crystallogr. B28 (1972) 60–76, https://doi.org/10.1107/S0567740872001876.

[71] S.C. Abrahams, Structure relationship to dielectric, elastic and chiral properties, Acta Crystallogr., Sect. A: Found. Crystallogr. 50 (1994) 658–685, https://doi.org/10.1107/S0108767394005738.

[72] J.F. Scott, Ferroelectrics go bananas, J. Phys. Condens. Matter 20 (2007), 021001, https://doi.org/10.1088/0953-8984/20/02/021001.

[73] P. Barrozo, D.R. Småbråten, Y.-L. Tang, B. Prasad, S. Saremi, R. Ozgur, V. Thakare, R.A. Steinhardt, M.E. Holtz, V.A. Stoica, L.W. Martin, D.G. Schlom, S.M. Selbach, R. Ramesh, Defect-Enhanced polarization switching in the improper ferroelectric LuFeO$_3$, Advanced. Matererials 32 (2020), 2000508, https://doi.org/10.1002/adma.202000508.

[74] L. Jin, F. Li, S. Zhang, S, Decoding the fingerprint of ferroelectric loops: comprehension of the material properties and structures, Progress in Advanced Dielectrics (2020) 21–104. April 2020.

[75] X.U. Min, Y.U. Yonggui, H. Zhang, W.A.N. Jiyang, Growth and characterization of ferroelectric Tb$_2$(MoO$_4$)$_3$ crystal, J. Rare Earths 27 (2) (2009) 192–195, https://doi.org/10.1016/S1002-0721(08)60218-5.

[76] C. Guzmán-Afonso, C. González-Silgo, M.E. Torres, E. Matesanz, A. Mujica, Structural anomalies related to changes in the conduction mechanisms of α-Sm$_2$(MoO$_4$)$_3$, J. Phys. Condens. Matter 25 (2012) 35902–36000, https://doi.org/10.1088/0953-8984/25/3/035902.